Dual-Polarization Measurements at C-Band Over the Ocean: Results From Airborne Radar Observations and Comparison With ENVISAT ASAR Data

Alexis A. Mouche, Danièle Hauser, Jean-François Daloze, and Christine Guérin

***Abstract*—This paper presents an analysis of measurements of the normalized radar cross-section (NRCS) in vertical and horizontal polarizations over the ocean obtained from the C-band airborne radar STORM. The dataset was collected during the experiment called "Validation with a Polarimetric Airborne Radar of Envisat SAR over the Ocean (VALPARESO)," which took place during the calibration/validation phase of the ENVISAT Advanced Synthetic Aperture Radar (ASAR). From this dataset, the properties of the polarization ratio are discussed and in particular its dependencies with radar geometry (incidence and azimuth angle) as well as with meteorological conditions (wind and sea state). The polarization ratio is found to be dependent on incidence and azimuth angles. Its dependence with incidence angle is found to be significantly different from empirical models previously proposed in the literature. It also exhibits some correlation with surface conditions (wind and wave) with a more important correlation with significant wave steepness. Two new analytical formulations are proposed to model the polarization ratio, one as a function of incidence angle only, the second one with additional dependence with azimuth angle. It is shown that it is necessary to consider an azimuth-dependent polarization ratio for incidence angles larger than 30°. Comparisons with the polarization ratio from ENVISAT ASAR images are used to assess this model.**

***Index Terms*—Normalized radar cross-section (NRCS), ocean surface, polarization difference, polarization ratio, synthetic aperture radar (SAR), wavebreaking, wind speed.**

I. Introduction

RADAR cross-section measurements of the ocean surface at moderate incidence angles are today commonly used to estimate ocean surface wind speed. Among the most well-known instruments, the scatterometer on the European Remote Sensing 1 and 2 (ERS-1 and ERS-2) satellites, have provided a tremendous volume of observations, which are operationally used for atmospheric or oceanic modeling. For these instruments, operating at C-band and VV polarization, empirical models have been developed to relate the radar cross-section measurements to the geometry of observations (incidence angle, azimuth angle with respect to wind direction) and wind speed. The most widely used empirical models are the CMOD-4 model developed at the European Center for Medium range Weather Forecast [1], and the CMOD2-IFR3 model [2] developed at Ifremer-France. Other scatterometers with a different radar wavelength (Ku-band) and a different geometry have been or are currently flying on other platforms (Seasat, NSCAT, Quickscat). For NSCAT and Quickscat, measurements are available in two orthogonal polarizations (HH and VV). Wind fields are operationally estimated using these instruments and empirical models developed specifically for the Ku-band [3], [4].

Since a few years, a growing interest is expressed for using the synthetic aperture radar (SAR) to estimate ocean surface wind, either because scatterometer are not so often implemented on satellite or because the horizontal resolution that can be obtained with the SAR is potentially very interesting for coastal applications. Indeed, the ENVISAT satellite (launched in 2002) has no scatterometer on-board, but an Advanced SAR (ASAR) operating at C-band and in horizontal (HH) or vertical (VV) polarization (or both). This ASAR is also versatile in its resolution and swath so that either a good coverage at medium resolution of the global oceans can be obtained or a high resolution of specific zones can be used (usually coastal zones). RADARSAT is the other available SAR presently flying on a satellite and which is used to document the ocean surface [5]. However, RADARSAT is only functioning in HH polarization, and this induces some difficulties because the empirical models of CMOD type have been established in VV polarization only. Their transposition to HH is still uncertain as indicated by the amount of recent or ongoing works on this subject [6]–[10] with some contradictions between the results of the different studies (see [9]).

In parallel to the development of instruments and empirical models, numerous studies have been devoted to build and test models based on physical backgrounds to relate the radar backscatter to the surface properties (wind, wave spectrum, statistics of surface roughness). These models are usually based on a spectral and statistical description of the ocean surface, characterized at least by the wave height spectrum, and the mean square slope of the surface (filtered at some characteristic scale), coupled with a simplified model describing the interaction between the electromagnetic wave and the surface. Description of the surface is usually based on physical backgrounds [10]–[12]. For the electromagnetic part, the composite surface theory has been widely used up to now. It consists in formulating the resonant Bragg backscattering due to short waves (wavelength of the order of the electromagnetic transmitted wave), tilted and affected in their hydrodynamics by the tilting longer waves (e.g., see [13]–[17]). Usually these models

Manuscript received July 22, 2004; revised November 17, 2004. This work was supported in part by the French Space Agency (CNES), in part by the Institut des Sciences de l'Univers (INSU), and in part by Météo-France in the context of the ENVISAT Validation Project AOE162 of the European Space Agency.

The authors are with the Centre d'Étude des Environnements Terrestres et Planétaires, Institut Pierre Simon Laplace, Centre for National Scientific Research (CNRS), F-78140 Velizy, France (e-mail: hauser@cetp.ipsl.fr).

Digital Object Identifier 10.1109/TGRS.2005.843951

also include a quasi-specular component, which dominates at small incidence angles, and is usually described by the physical optics approximation [18]. Although these models are widely used, they suffer from several drawbacks. In particular, it has been shown that they are not able to reproduce correctly the polarization ratio—ratio of the radar cross-sections in VV and HH polarizations [11], [17], [19]. They also suffer from the limitations in their formulation (*a priori* choice of a scale-dividing wavenumber separating short-scale Bragg resonant waves from larger tilting waves). This led Voronovich and Zavarotny to propose an alternative formulation of the electromagnetic part of the model based on the small slope approximation [20].

Several attempts have been done to improve such models, in order to obtain a better agreement between models and observations. Kudryavstev *et al.* [11] have introduced wavebreaking effects in both the surface description and the backscattering model. This model has been constructed by using a physical representation of the surface and of the surface/electromagnetic interactions with some parameters fitted using values of the polarization ratio available in the literature at different radar wavelengths. Hence, intrinsically, this model should be compatible with both HH and VV measurements of the radar cross-section. However this model was built with a limited available dataset. Using a slightly different approach, Wackerman *et al.* [10] have chosen to adapt to the HH polarization a two-scale model developed (without considering breaking effects) and fitted for VV polarization. The proposed modifications concern the surface description only (shape of the wave spectrum, description of the hydrodynamic modulation). Based on results in a wave tank, Plant [21] proposed to account for Bragg scattering from bound tilted waves, but he also showed [22] that in real conditions on the ocean surface, this is not sufficient to explain the difference in the backscatter in HH and VV polarizations at large incidence, and that sea spray may play an important role.

In this context, the study presented in this paper is aimed at a better description of the C-band radar polarization ratio (VV/HH radar cross-section) and at the HH-polarized radar cross-section as a function of the radar geometry (incidence angle azimuth angle) and of the surface or interface characteristics (wind, waves). The study is based on observations, collected with a C-band polarimetric airborne scatterometer (STORM radar developed at the Centre d'Étude des Environnements Terrestres et Planétaires (CETP); see Section II-A), during the experiment called Validation with a Polarimetric Airborne Radar of the Envisat SAR over the Ocean (VALPARESO). This experiment was carried out in October–November 2002 over the Atlantic and British Channel near the coasts of France and Great Britain. It was coordinated with the ENVISAT ASAR calibration and validation phase. During VALPARESO, airborne observations with STORM have been acquired simultaneously with ENVISAT ASAR passages in different modes of incidence and polarization (including some dual-polarization modes). Flights over a meteo/oceanic buoy provided the coincident wind and wave conditions.

From this set of data we present here an analysis of the measured polarization ratio as a function of incidence angle (in the range 20° to 45°), wind speed (ranging from 4–16 $\mathrm{m \cdot s^{-1}}$), and wave conditions (significant wave height from 0.5–5 m). The observing geometry of STORM (with an antenna scanning over 360° around the vertical axis) allowed us also to investigate the behavior of the radar cross-section in VV and HH (and of the polarization ratio) as a function of azimuth direction with respect to the wind direction. This point has not been much investigated before, except in the study of Unal *et al.* [23]. Our experimental dataset is also compared to different models of polarization ratio [6]–[8], [11], [24], and used to propose two different analytical formulations of the polarization.

In Section II, we present the VALPARESO experiment, the characteristics of the STORM instrument, and describe the dataset used in the present study. In Section III, we show the results obtained for the polarization ratio, as a function of incidence angle, compare it with models proposed by other authors, and discuss the dependence of this ratio with wind speed, wind direction, and sea state. In addition, the difference of the NRCS in VV and HH is also investigated. From this analysis, two analytical models are proposed in Section IV for the polarization ratio, one with, and the other without the azimuth angle as a parameter. They are built for an easy application on HH-polarized radar cross-section observations in order to estimate equivalent VV-polarized data, which can then be inverted in terms of wind by using a CMOD-type empirical model. In Section V, differences between these two models are discussed. In Section VI, we present an independent validation of our models by analyzing dual-polarized ASAR data of ENVISAT. Finally the main conclusions are given in Section VII.

II. VALPARESO EXPERIMENT

The VALPARESO experiment was carried out by CETP, in collaboration with IFREMER and Météo-France, in the context of the ASAR geophysical calibration and validation exercise performed and supported by the European Space Agency (ESA) after the launch of ENVISAT. Three main objectives were defined for VALPARESO: 1) contribute to the validation and improvement of the inversion methods implemented by ESA for the inversion of SAR imagetts in terms of wave spectra; 2) contribute to a better knowledge of the normalized radar cross-section over the ocean at various polarization states and geometrical configurations and its relation with surface parameters; and 3) investigate the potentiality of full polarimetric measurements over the ocean. Here we focus on the second point only. Results on the other objectives will be published separately.

The VALPARESO experiment took place from October 19 to November 21, 2002 off the coasts of France and the U.K. (near-Atlantic coasts of France and English Channel). The main component of this experiment was the airborne radar called STORM. The characteristics of STORM have been described elsewhere in details (see [25]), but are summarized below.

Fig. 1 shows the experiment area and a typical flight trajectory of STORM. During VALPARESO, ASAR images for 20 different tracks and different configurations had been requested to ESA. However, due to problems in the ENVISAT mission ground segment, only ten of them could be provided by ESA. Two of them, corresponding to a dual-polarization acquisition mode (HH and VV) are used in the present study. The processing of these SAR data is detailed in Section II-C.

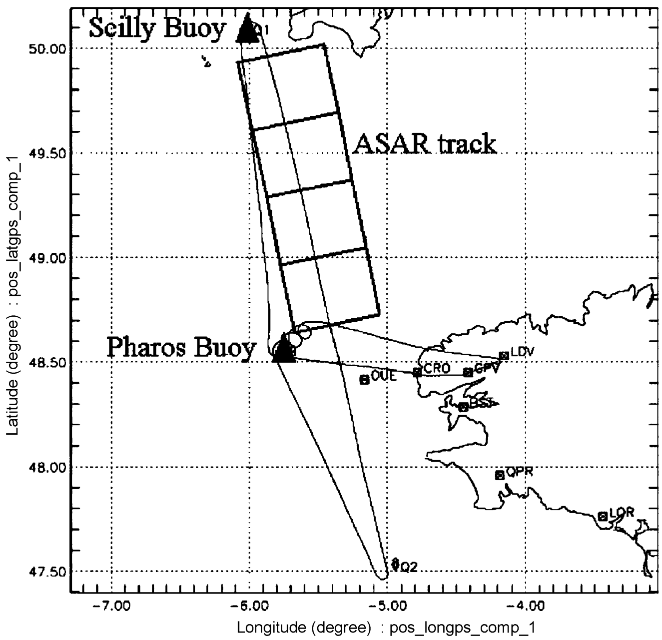

Fig. 1. Example of a typical flight with STORM onboard Merlin IV. In this case, the airplane flew over the 2 buoys (Pharos and Scilly) and along the ASAR swath (shown as the rectangles).

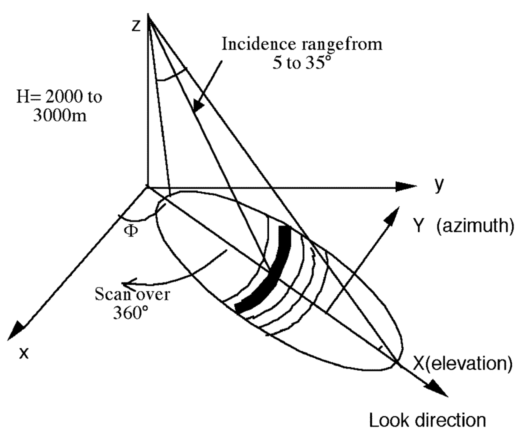

Fig. 2. Geometry of observations with STORM. The flight level ranges from 2000–3000 m, corresponding to footprint sizes of (1200 m × 280 m) to (1800 m × 420 m).

In the experimental zone, two meteo-oceanic buoys were frequently overflown by STORM and/or ENVISAT ASAR. The first one is the "PHAROS" Buoy ($48^\circ 31' 42''$N, $5^\circ 49' 03''$W); it provided measurements of wind and ocean wave spectra for the whole duration of the campaign with a 1-h sampling frequency. The second one is a British buoy of the operational network located near the Scilly Islands ($50^\circ 04'$N, $06^\circ 04'$W). This latter is not used in the present study.

A. STORM Observations

STORM uses a frequency-modulated continuous-wave (FM/CW) transmitted wave form. It transmits every 8 ms alternatively in H and V polarization and receives simultaneously in both H and V channels (see [25] for the details). The geometry of STORM observations is presented in Fig. 2. Because the microwave signal is transmitted continuously, a dual-antenna system is necessary with one antenna for transmission, and one for reception. This set of two antennae is mounted in a radome placed under the airplane fuselage and has the capability to rotate over 360° in the horizontal plan, alternatively clockwise and counterclockwise. As mounted for VALPARESO on the MERLIN-IV aircraft of Meteo-France [26], the antenna points toward the surface with an incidence angle (with respect to nadir) of 20°, when the airplane is horizontal. The 3-dB two-way beam aperture is $\pm 15^\circ$ in elevation and $\pm 3.8^\circ$ in azimuth. The antenna system can be controlled either to scan over 360° around the vertical axis at a rate of three rotations per minute or to stop at a fixed azimuth angle. The range resolution is 1.53 m, corresponding to a horizontal resolution in the elevation direction of 4.5 m at 20° incidence. The aperture in the azimuth direction is used with its real dimension (no synthetic aperture processing), so that the signal is integrated over the azimuth footprint (typically a few hundred of meters for flight levels between 2000 and 3000 m). This configuration was chosen to estimate the directional ocean wave spectra according to the method previously developed with our monopolarized (HH) airborne radar RESSAC [27]. It is also well suited to analyze the normalized radar cross-section characteristics as discussed in the present study.

Isolation between polarization is better than 30 dB for the transmitting antenna, and 40 dB for the receiving antenna. Isolation between transmitting and receiving in the copolar condition is better than 70 dB. This ensures a good quality of the analysis of the radar cross-section in different polarization states.

Different acquisition modes of STORM data have been used during VALPARESO. They differ by: 1) the flight level (around 2000 or around 3000 m); 2) the possibility to choose (or not) an incoherent real-time integration; and 3) the flight patterns: either in straight line which corresponds to a mean incidence angle of observation at 20° (and an incidence range from 5° to 35°), or in circle patterns performed with a 15° roll of the aircraft and the antenna fixed on one side so as the mean incidence angle is about 35° (and the incidence range 20° to 50°). This latter mode in circle patterns was used in the vicinity of the PHAROS buoy location.

The data recorded by the system provides the backscattered power as a function of range (see below), either every 8 ms (alternatively in HH and VV) or every 128 ms, after real-time integration over eight samples for each polarization. Ancillary data from the radar and from the aircraft were recorded at the same rate (roll, pitch, drift angles, speed, latitude, longitude, etc.) from the inertial navigation system of the aircraft. The chosen sampling rate of 128 ms corresponds to observations (in HH, HV, VH, VV) every 2.3° in azimuth when the antenna rotates at the nominal rate of three rotations per minute (horizontal flight patterns). For the circle flight patterns, the same integration time corresponds to one observation every 1.2° accounting for a 40-s duration for a circle with the aircraft. In the following, only HH and VV observations are discussed.

Table I shows the list of the 16 STORM flights used in the present study along with the range of incidence covered by STORM.

B. STORM Data Processing

The raw data recorded by the STORM system consists in the power spectrum of the backscattered signal (or amplitude and

TABLE I
LIST OF STORM FLIGHTS WITH THEIR ASSOCIATED CONDITIONS OF INCIDENCE, WIND SPEED, WIND DIRECTION, SIGNIFICANT WAVE HEIGHT (H_s) AND PEAK WAVELENGTH (λ_{peak}) AND SEA–AIR TEMPERATURE DIFFERENCE (SST-AIRT). THE RANGE OF VALUES INDICATED FOR WIND, SEA-STATE, AND TEMPERATURE DIFFERENCE CORRESPONDS TO THE MINIMUM AND MAXIMUM VALUES RECORDED DURING THE FLIGHT (2 TO 3 h)

				Information given by Pharos Buoy				
Sensor	Flight number	Date	Incidence Range[°]	Wind Speed [m s^{-1}]	Wind Direction [°/North]	Hs [m]	λ_{peak} [m]	SST-AirT [°]
STORM	Flight 12	2002/10/19	10-48°	9.7-10.8	126-127	0.7	78-86	2.1 to 1.8
STORM	Flight 13	2002/10/20	10-36°	12.4	120	2.9	-	0.2 to -0.4
STORM	Flight 14	2002/10/20	10-49°	10.3	152	2.6	230	-1.3 to -1.5
STORM	Flight 15	2002/10/23	9-49°	11.3	298	3.0	116	1.2 to 2.2
STORM	Flight 16	2002/10/23	10-48°	7.6	221	1.8	75	1.0 to 0.7
STORM	Flight 17	2002/10/26	9-49°	6.5-7.0	212-222	3.3	185-188	-0.9 to 1.0
STORM	Flight 18	2002/10/29	9-46°	4.9-5.4	203-206	1.3	81-82	-1.1 to -1.2
STORM	Flight 19	2002/10/29	9-41°	3.2	193-194	0.9	49	-1.2 to -1.3
STORM	Flight 20	2002/11/03	23-51°	14.0	181	3.9	159	-0.6 to -0.9
STORM	Flight 21	2002/11/04	10-46°	4.9-5.9	275	3.3-3.8	221-232	-0.6 to -0.9
STORM	Flight 22	2002/11/11	10-50°	10.8	206-249	3.3	105	-0.4 to -0.8
STORM	Flight 23	2002/11/11	10-50°	10.3-11.9	266	4.1	214-329	-0.7 to -0.2
STORM	Flight 24	2002/11/14	10-52°	14.6	221-259	3.7	145	-0.0 to0.5
STORM	Flight 25	2002/11/17	10-46°	4.3-5.4	230	1.1-1.4	140-150	2.5 to 2.2
STORM	Flight 26	2002/11/17	10-44°	4.3	327-337	1.0	130	2.1 to 1.4
STORM	Flight 27	2002/11/20	10-51°	15.1-15.7	207-211	2.6	262-265	0.7 to 0.4

phase in the polarimetric nonintegrated mode) as a function of the beat frequency (corresponding to the frequency of the signal obtained after filtering of the mixed signal between transmitted and received signal). This beat frequency f_b is related to the two-way distance $(2R)$ between radar and scatter by the following relationship:

$$f_b = 2R\frac{B}{cT} + \delta_D \tag{1}$$

where B is the transmitted bandwidth, T the duration of the transmitted signal, c the speed of light, and δ_D is a Doppler effect correction to be taken into account due to the aircraft speed.

The flight altitude H is estimated from the spectrum itself as the distance of the first peak in the backscattered signal.

The relation between distance in range (R) and incidence angle θ is then applied $(\cos\theta = H/R)$ to obtain a power spectrum versus incidence angle with a resampling in 1° incidence bins.

For the analysis presented here, all the data correspond to power spectrum integrated over 128 ms (either in real-time or during the postprocessing).

To obtain NRCS, from the measured backscattered power, the radar equation is applied (e.g., see [28]), taking into account the antenna gain, antenna gain pattern, instrument losses, range spreading loss. Antenna gain and gain pattern were provided by the manufacturers of the antenna. In order to correct for the antenna gain pattern while taking into account perturbations due to aircraft attitude changes, the antenna gain pattern correction was calculated and tabulated for all combinations of roll, pitch, and azimuth angle of the antenna.

The final product used in the present analysis is as follows:

—VV and HH NRCS for incidence angles from 10° to 35° every 2.3° in azimuth for the horizontal straight flight patterns;

—VV and HH NRCS for incidence angles from 20° to 50° every 1.2° in azimuth for the circle flight patterns.

The effective upper limit of the incidence range as described just above and considered in the following was chosen by limiting the analysis to NRCS values that were at least 3 dB over the noise level. Depending on the wind conditions, flight level, and acquisition mode, the upper incidence angle useable for this study ranges in fact from 35° to 50°.

Calibration is an important issue for NRCS analysis. Although we concentrate in the following on the polarization ratios (VV/HH), which is not very sensitive to the absolute calibration of the radar (if the receiver chains are equivalent), we paid also much attention to the calibration of each polarization chain.

The internal calibration procedure of STORM is based on laboratory measurements using an optic delay-line integrated in the radar system, a noise signal, and a control of the transmitted power. Estimation of the receiver gain from the internal calibration showed that the two receiving channels (for H and V polarization) are well balanced with only a 0.2-dB difference in gain. The gain stability was checked through long-term measurements (using a known noise source).

In addition, flights over artificial targets (corner reflectors of dihedral and trihedral shape) have been performed to check the absolute calibration (including antenna effects). The procedure was to fly over five trihedral and one dihedral corner reflectors installed on an aircraft runway. This combination of dihedral and trihedral corner reflectors was designed for the full polarimetric calibration [25], but was also used for the amplitude calibration. All the reflectors were installed in such a way that for each radar measurement and for the optimal flight-altitude (470 m), all of them were included in the radar footprint. When positioning the antenna in the forward direction (parallel to the aircraft), this allows to measure the corner reflectors response at different incidence angles at the same time. The radar cross-section maximum value is obtained close to the center of the antenna beam in the elevation direction.Table II shows the obtained radar cross-section of the trihedral reflector for three passages over the runway performed a few days before the be-

TABLE II
MEASURED CROSS-SECTION OVER TRIHEDRAL REFLECTORS IN DECIBELS DURING THE VALPARESO FIELD EXPERIMENT CALIBRATION STEP

	Measured radar cross-section in HH (dB)	Measured radar cross-section in VV (dB)	VV/HH (dB)
Trihedral-Pass 1	32.4	32.1	-0.3
Trihedral-Pass 2	32.0	32.1	-0.1
Trihedral-Pass 3	32.6	32.3	-0.2

ginning of the experiment. These values must be compared to the 32.5-dB theoretical expected values for our corner reflectors. Our radar cross-section values deviate from the theoretical value by less than 0.5 dB in HH and less than 0.4 dB in VV. Taking into account the uncertainty of such measurements due to the difficulty of alignment of the radar beam with the reflectors, it is not possible to conclude that it is a systematic bias of our NRCS value. The corresponding maximum deviation for the VV/HH polarization ratio is -0.3 dB.

In order to relate our NRCS data to the sea surface conditions, we limit our analysis of the STORM data to files acquired close to the PHAROS buoy ($\pm 0.2^\circ$ in latitude and longitude from the buoy position). The radar cross-section and polarization ratios of each case observed by STORM and discussed in the following are representative of a scale of about 10 km $\times$ 4 km in the rectilinear flight mode and 5×5 km in the circular flight mode. It corresponds to an analysis of raw data over about 1.5 min (respectively 3.3 min) for the rectilinear (respectively circular) flight mode.

C. ASAR Dataset and Processing

During VALPARESO, the C-band ASAR aboard ENVISAT was programmed to acquire image in the so-called IS1, IS2, and IS3 swath modes. These modes correspond respectively to incidence ranges of 14° to 22°, 18° to 26°, and 25° to 31° perpendicular to the flight direction. Depending on the orbit, our request was to get either the so-called IMS or APS products. IMS corresponds to acquisition of singe-look complex images in a single polarization (either HH or VV); APS corresponds to the alternate polarization mode, which provides two images from the same scene with a combination of two polarizations (HH and VV or HH and HV or VV and VH). The images cover a zone 80–100 km wide (depending of the incidence mode). The coverage in the azimuth direction is variable and reaches hundred of kilometers (200–400 km depending of the cases). The intrinsic pixel resolution is about 7 m in range and 3 m in azimuth direction (7 m for APS mode). On the whole campaign we got ten datasets. Two of them are in APS mode and IS3 incidence range (25° to 31°). To complement this small dataset in HH/VV polarization, we also use APS images acquired over North Pacific and North Atlantic Oceans at larger incidence angles (see Table III).

In order to estimate the NRCS, the products provided by ESA have been corrected for range spreading loss, elevation antenna pattern, and absolute calibration constant. The range spreading loss is a geometric effect due to the variation of the range distance (i.e., incidence angle) inside the APS image. For each polarization and at each incidence angle, the correction for antenna gain pattern was fixed from the auxiliary file delivered by ESA. The absolute calibration constant given in the data files were used to calculate the NRCS, but it does not affect the polarization ratio, since its value is the same for both polarizations.

TABLE III
ASAR DATASET

Sensor	Orbit	Frame	Date	Incidence mode/angle [deg]
ASAR	03469	409	2002/10/29	IS3~26-30
ASAR	03748	187	2002/11/17	IS3~26-30
ASAR	07043	476	2003/07/06	IS6~39-42
ASAR	07358	290	2003/07/28	IS7~42-45
ASAR	08236	166	2003/09/27	IS4~31-36
ASAR	08970	399	2003/11/17	IS2~19-26
ASAR	10483	409	2004/03/02	IS7~42-45
ASAR	10793	218	2004/03/24	IS3~26-30
ASAR	11213	137	2004/04/22	IS4~31-36

For the present analysis, the NRCS of the ASAR images were calculated as mean values over 256 pixels in range and 512 pixels in azimuth i.e., over 2 km $\times$ 1.5 km.

III. RESULTS

Tables I and III summarize the VALPARESO and ENVISAT ASAR datasets. For the VALPARESO dataset (Table I), the corresponding surface and atmospheric conditions as given by the PHAROS buoy are also indicated (estimate every hour of the omnidirectional wave spectrum, wind, air, and sea surface temperature-averaged over a 10-min period for these latter). It is interesting to note that the meteorological conditions relative to our dataset cover a large range: wind speed from 4–16 $\mathrm{m \cdot s^{-1}}$, wave height from 0.7–4.1 m.

In the following, we will discuss results of the polarization ration P defined as

$$P = \frac{\sigma_0^{VV}}{\sigma_0^{HH}} \tag{2}$$

where σ_0^{VV} and σ_0^{HH} are the NRCS values in VV and HH polarization, respectively, expressed in linear units. The polarization ratio P is expressed hereafter either in logarithmic units (decibels) or in linear units.

We also will discuss results of the polarization difference D defined as

$$D = \sigma_0^{VV} - \sigma_0^{HH} \tag{3}$$

where D, σ_0^{VV}, and σ_0^{HH} are expressed in linear units.

In Section III-A, the polarization ratio P is first analyzed as a function of incidence angle. Then, we study in Section III-B and C the influence on P of wind (speed and direction) and sea state (wave height and wave steepness). Finally in Section III-D, we present complementary results on the polarization difference D.

A. Polarization Ratio Versus Incidence Angle

The mean polarization ratio P obtained from STORM in the upwind direction as a function of incidence angle θ is shown in Fig. 3. In this plot, the mean values correspond to the average over all cases described in Table I, and the vertical bars indicate the standard deviation from this mean value, due to scatter

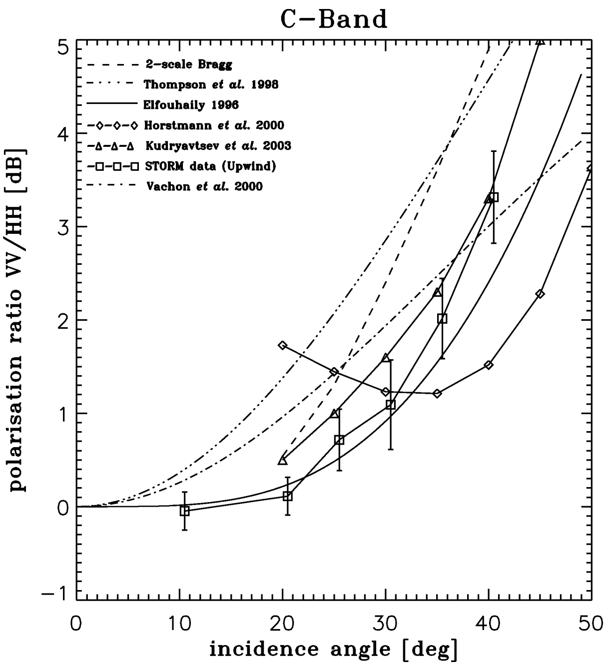

Fig. 3. Averaged polarization ratio in the upwind direction versus incidence angle. The results from STORM are indicated as the solid line without symbol and with the error bars (standard deviation from the mean). Various models of the literature are also plotted (see legend on the plot and text).

within the dataset. In this figure are also plotted classical representations of the polarization ratio that can be found in the literature (see below).

The results from STORM (solid line with error bars in Fig. 3) indicate that between 10° and 20°, the polarization is almost constant and close to 0 dB, meaning that the NRCS in VV is equal to the NRCS HH. At incidence angles larger than 20°, the polarization ratio increases significantly with incidence angle, reaching more than 3 dB at 40° incidence angle. Note that the results for STORM over the incidence range of 10° to 42° has been obtained by combining the two different modes of observations (rectilinear flights and circle flights). From this combination, data cover two ranges of incidence angles which overlay in the 20° to 35° range. The data from the two modes are averaged in Fig. 3. The results show a good continuity over the whole incidence range with, however, a maximum of standard deviation in the intermediate range of incidence angles, probably due to the average of observations from the two different modes of observations.

The other relationships plotted in Fig. 3 are those from Thompson *et al.* [6] (dashed-triple dotted line), Vachon and Dobson [8] (dashed-dotted line), Horstmann *et al.* [7] (line with diamond symbols), Kudryavstev *et al.* [11] (line with triangle symbols), Elfouhaily [24] (solid line), and from a two-scale Bragg model as described also in [11] (dashed line).

Comparison with the polarization ratio corresponding to the two-scale Bragg model (model taking into account Bragg backscattering modified by local-tilting and hydrodynamic effects due to longer-underlying waves; see [11]) shows that this latter overestimates considerably the observed polarization ratio. Since the two-scale Bragg polarization ratio is smaller than the pure Bragg one (e.g., see [11]), we conclude that there is no possibility that a Bragg modeling will be able to reproduce the observations. According to our observations, the Kirchhoff value ($P = 0$ dB)—not plotted—is valid only up to incidence angles of about 20°, where quasi-specular reflection dominates. In the 20° to 45° range, the observed polarization ratio lies between the two limiting curves of Bragg and Kirchhoff but departs significantly from both.

Thompson *et al.* [6], proposed the following relation between P and the incidence θ:

$$P = \frac{(1+2\tan^2\theta)^2}{(1+\alpha\tan^2\theta)^2} \tag{4}$$

where P is expressed here in linear units, and α is a constant equal to 0.6. This relationship was proposed to keep a general form consistent both with the Bragg condition ($\alpha = 0$) and the geometrical optics (or Kirchhoff) condition ($\alpha = 2$). The value of $\alpha = 0.6$ was chosen in [6] from an analysis over a limited set of RADARSAT observations (in HH polarization). This value was later also recommended by Monaldo *et al.* [9] from the analysis of a larger set of RADARSAT data (in HH) and *in situ* data. Fig. 3 shows that the formulation proposed by [6] overestimates significantly our observations over the whole range of incidence angles and by more than 1.5 dB at 35°.

Elfouhaily [24] proposed this expression

$$P = \frac{(1+2\tan^2\theta)^2}{(1+2\sin^2\theta)^2}, \qquad \text{[linear unit]}. \tag{5}$$

Elfouhaily obtained this formulation by transposing to the horizontal polarization the effective scattering Fresnel coefficient for vertical polarization. This latter was deduced from a first order development of the scattered field for a slightly rough and gently tilted surface in the framework of the small perturbation method (e.g., see [18]). In [24], it was shown that this new expression of the effective Fresnel scattering coefficient yields NRCS values in HH-pol in better agreement with the SASS-2 model (in Ku-band) than the classical one. This is confirmed by the rather good agreement visible in Fig. 3 between our observations and the curve from the study of [24]. In particular, this model reproduces quite well the fact that the polarization ratio is close to 0 dB up to 20° incidence, and then increases with incidence angle. Among the different models plotted in Fig. 3, Elfouhaily model is one of the closest to our observations, in spite of the small underestimate of the polarization ratio, which increases slightly with incidence.

Results for the model proposed by Kudryavtsev *et al.* [11] are plotted in Fig. 3, for the following conditions: 10-m $\cdot$ s^{-1} wind speed and upwind direction of observation. The model is based on the idea that other effects than the Bragg scattering mechanism and local-tilting and/or hydrodynamic effects due to longer-underlying waves have to be taken in account to explain polarization ratio values. In their model, Kudryavtsev *et al.* [11] introduced a term of quasi-specular reflection from very rough wavebreaking patterns, which were described according to the wavebreaking statistics proposed by Phillips [29]. With their approach, the polarization ratio depends not only on incidence angle, but also on wind speed and azimuth angle. We will discuss this dependency further down. The empirical constants of this model were fitted by using historical data at different radar wavelengths [11]. The model was assessed by comparing with the NSCAT Ku-band results [30], a small set of X-band data collected from a previous experiment performed by our group [31], and some C-band empirical models mainly obtained from RADARSAT. Here we compare our STORM dataset with the Kudryavtsev *et al.* [11] model as described in their paper. Both the trend and the values with this model are in rather good agreement with our measurements, in spite of a small overestimation of the polarization ratio by the model.

The relation proposed by Horstmann *et al.* [7] was deduced from a comparison between NRCS obtained from five C-band ScanSAR images in HH polarization, and observations of the C-band ERS-2 scatterometer in VV polarization, collocated in space and time. As shown in Fig. 3, The shape of the curve found by [7] presents a minimum value at incidence angle close to 35°, which is in disagreement with all other formulations. However, it cannot be excluded that at moderate incidence angles, their results are affected by the ADC saturation existing on ScanSAR RADARSAT data at near-range. This problem was illustrated among others by Monaldo *et al.* [9] for incidence angles up to 25°, and also mentioned in [7]. At incidence angles larger than 35°, the curve of [7] shows the same trend as the STORM curve with incidence but present much lower values of P.

The results of Vachon and Dobson [8] were obtained by comparing observed values of NRCS in HH polarization from RADARSAT-1 with values of NRCS in VV polarization estimated from *in situ* wind measurements and the empirical CMOD2-IFR3 model [2] from IFREMER. They showed that the analytical formulation expressed in (4) with $\alpha = 0.6$ lead to a wind speed overestimate (especially for high wind speeds). They recommended the same formulation but with $\alpha = 1$. As shown in Fig. 3, their relation is in agreement with our results for incidence close to 35°, but it underestimates significantly our observations at larger incidences, and overestimates them at smaller incidences.

Finally, we compare in Fig. 4 the polarization ratio obtained from STORM in two cases of observations (October 29, 2002, and November 17, 2002) with the ENVISAT ASAR polarization ratio obtained over the same area and nearly at the same time. Both cases correspond to light and steady wind conditions ($4.9\ \mathrm{m} \cdot \mathrm{s}^{-1}$ at 11:00 UTC at the PHAROS buoy location on October 29, $4.3\ \mathrm{m} \cdot \mathrm{s}^{-1}$ at 22:00 UTC on November 17). We observe that the polarization ratio P from STORM and ASAR measurements are very close in their common range of incidence angles. Although wind speed is quite similar in both cases, the polarization ratio differs significantly (up to 1 dB) from one case to the other. We will see below that this may probably be attributed to different sea-state conditions.

To summarize these comparisons, we have shown that the polarization ratio as a function of incidence angle obtained from STORM differs significantly from the previously proposed empirical function [6]–[8]. Most of these empirical functions were obtained by using HH-polarized observations of RADARSAT and are therefore sensitive to a calibration error of this radar. The influence of a possible calibration error or shift in incidence angle was discussed in [9] and shows that this may explain the different values of the α coefficient of (4) found in the literature. Here our results are not sensitive to a possible overall calibration error since HH- and VV-polarized data of STORM have been acquired simultaneously with a careful assessment of the polarization of each channel (see Section II). Concerning the comparison of STORM results with theoretical models, we confirm: 1) that the Bragg model (even two-scale Bragg) is unable to reproduce the polarization ratio; 2) that the Kirchhoff assumption, which leads to a constant ratio of P equal to 1 is only valid up to about 20°. Two recent models based on physical backgrounds seem appropriate to reproduce the polarization dependence with incidence angle: the model proposed by Elfouhaily [24] and the one proposed by Kudryavtsev *et al.* [11], although modifications in the choice of some constants could improve the agreement with our observations. The theoretical background of these two models is quite different and it is not the purpose of this paper to choose one of them and improve them. More detailed comparisons of our results with physically based models will be proposed in a separate publication.

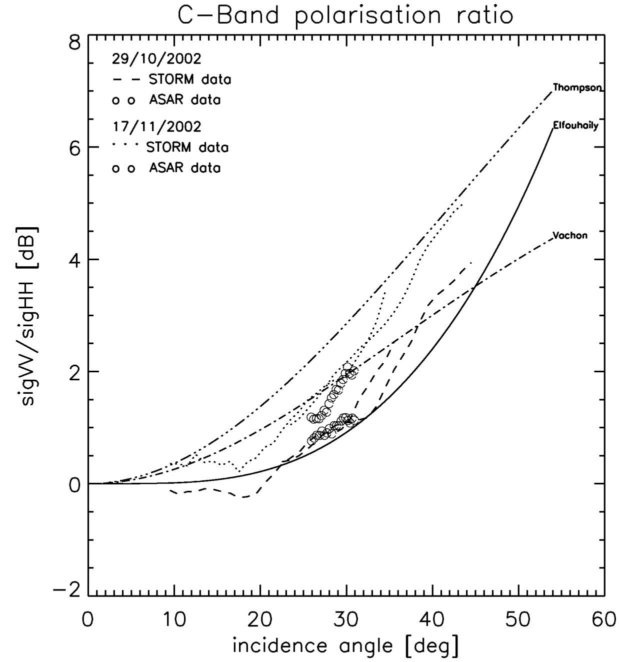

Fig. 4. Polarization ratio measured by STORM and by ASAR onboard ENVISAT for two cases of low wind speed. Models of [6] (dashed-triple dot), [8] (dashed-dotted line), and [24] (solid line) are superimposed on the plot.

B. Wind Influence

Fig. 3 shows that the scatter of the polarization ratio P around its mean value may reach up to 1.5 dB. In this section, we investigate whether this scatter may be due to wind variations.

1) Wind Speed: First we analyze the behavior of the NRCS in each polarization with wind speed. Fig. 5 shows the NRCS in VV [Fig. 5(a)] and HH [Fig. 5(b)] polarizations as a function of wind speed, for three incidences angles (20.5°, 30.5°, and 40.5°). In this figure and further down, wind speed was converted from the measured values to equivalent winds at 10 m height in neutral conditions, using the COARE algorithm [32]. The dependence in wind speed is obvious for HH and VV polarizations, as expected. In Fig. 5(a), the CMOD2-IFR3 model [2] is also plotted. The agreement between the STORM data and this model is quite good, particularly at medium and large inci-

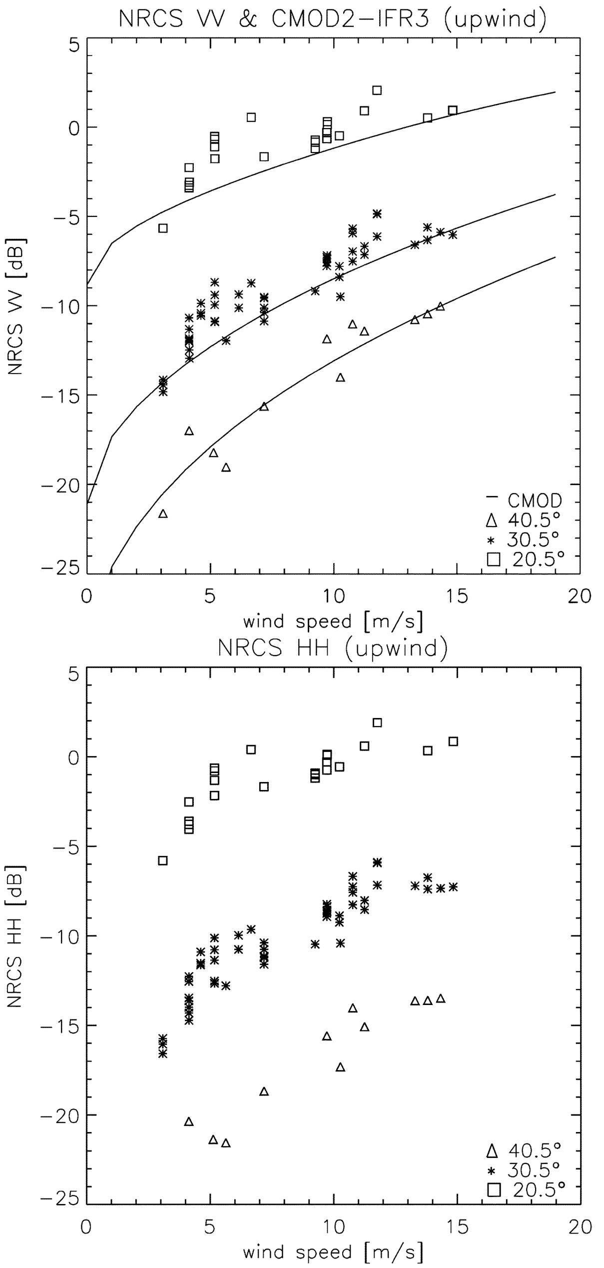

Fig. 5. (a) Normalized radar cross-section versus wind speed measured by STORM in the upwind direction, for three incidence angles: 20.5° (squares), 30.5° (stars), and 40.5° (triangles). Solid lines represent the CMOD-IFR3 model for the three incidence angles. (b) Same as (a), but in HH polarization.

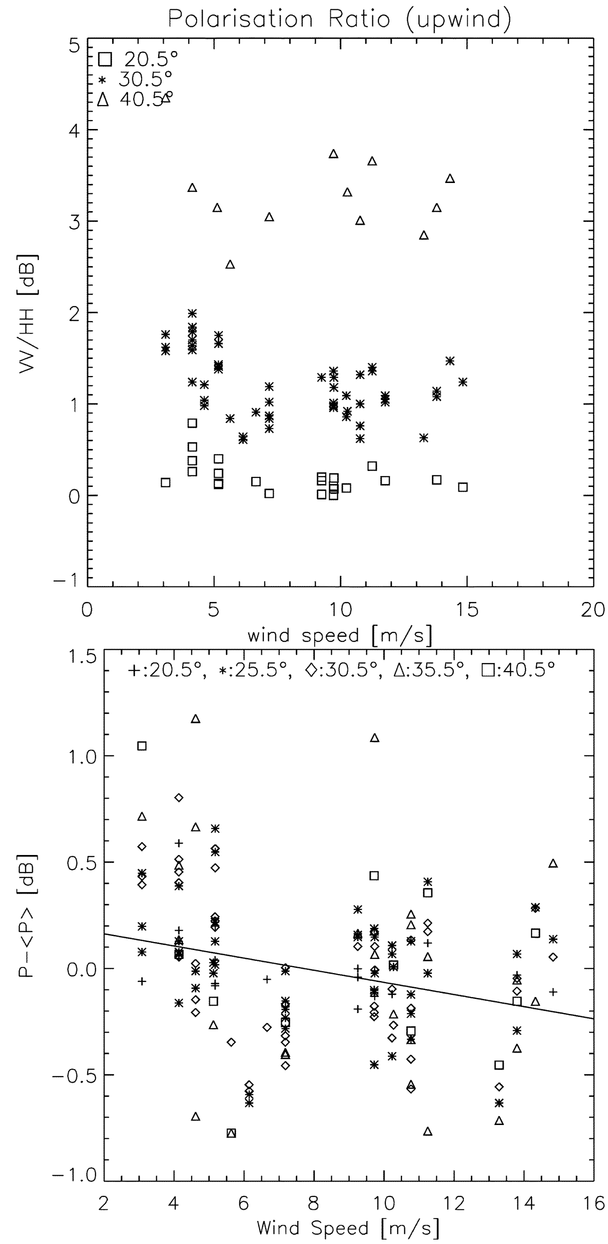

Fig. 6. (a) Same figure as Fig. 5(a) but for the polarization ratio. (b) Deviation of the polarization ratio with respect to its mean value at each considered incidence angle (20.5°, 25.5°, 30.5°, 35.5°, and 40.5°), as a function of wind speed. A different symbol is used for each incidence angle (see on the plot). The line corresponding to a linear fit is plotted as a solid line. The correlation coefficient is 0.27 in this case.

dence angles. At small incidence angles (less or equal to 20°), the VV values of the radar cross-section are slightly smaller than the CMOD2-IFR3 model. For this range of incidence angles, deviations from the CMOD2-IFR3 model are not really surprising because the model reaches its limit of validity (CMOD2-IFR3 was established for incidence angles from 18° to 58°). Fig. 5(b) for HH polarization shows the same general trend as Fig. 5(a) for VV polarization.

The polarization ratio versus wind speed is shown in Fig. 6(a) for the same three incidence angles (20.5°, 30.5°, and 40.5°). In agreement with what was shown in Section III-A, this figure shows different levels of P depending on the incidence angle. Variation of P with wind speed is quite small, in agreement with what was shown in [10].

In order to increase the number of points in this analysis, while taking into account the dependence of P with incidence, we also analyzed the linear correlation between the deviation of P from its mean value at each incidence, and wind speed [Fig. 6(b)]. The correlation coefficient is 0.27. A test of null hypothesis based on a random selection of the wind parameter (random procedure repeated 10 000 times) shows that this value of correlation is significant at the 99% confidence level. Hence, there is indeed a linear relation between P-$\langle P\rangle$ and wind speed but with a low correlation (0.27).

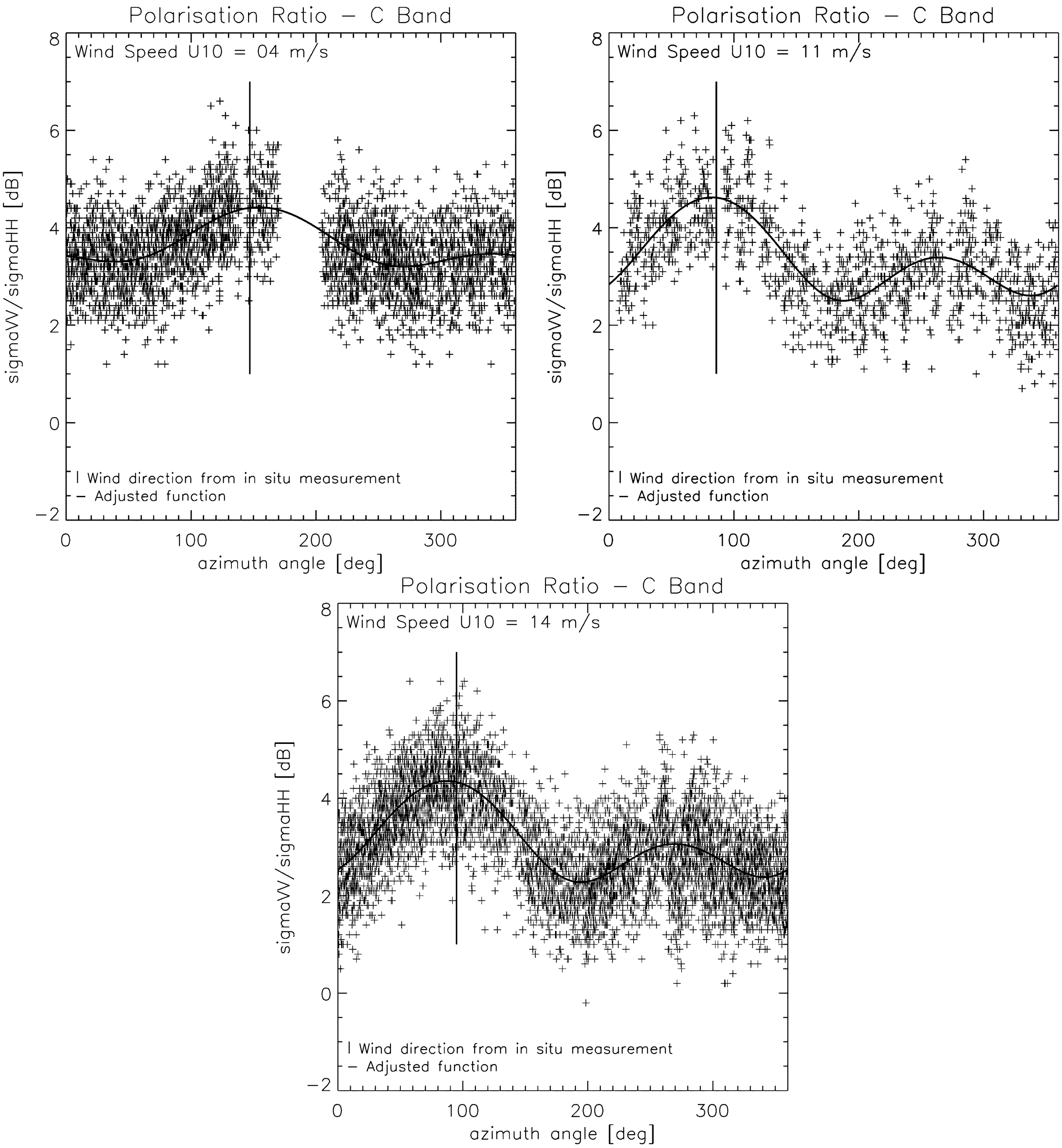

Fig. 7. (a) Polarization ratio versus azimuth angle for 40.5° incidence angle. The heavy solid line represents the fit of (6) to the data. The vertical line represents the downwind direction given by the Pharos Buoy when it was flown over by the Merlin IV with STORM. This case corresponds to light wind (4 m $\cdot$ s^{-1}). (b) Same figure as (a) but for a different wind speed case (11 m $\cdot$ s^{-1}). (c) Same figure as (a) and (b) but for a different wind speed case (14 m $\cdot$ s^{-1}).

2) Wind Direction: The variation of the NRCS with the azimuth angle (angle between wind direction and radar look direction) is a well-known characteristics explained by the anisotropy of the energy density of the short Bragg waves. Empirical models like the "CMOD" type models [1], [2] reproduce these characteristics. This is a feature that is still difficult to represent with physically based models, because the anisotropy of the short waves is not well known nor well represented by the hydrodynamic part of these models.

Fig. 7 presents for three selected cases of our STORM observations (at low wind, moderate wind, and high wind conditions), the polarization ratio P (in decibels) as a function of azimuth angles, for the incidence angle of 40.5°. We clearly observe a modulation of the polarization ratio with azimuth angle. Note that the wind direction measured at the PHAROS buoy—wind blowing from—is plotted as a vertical solid line in Fig. 7(a)–(c). In order to represent analytically this modulation and analyze its behavior with azimuth angle incidence angle and wind speed, a truncated Fourier series as given in (6) has been fitted to the data points

$$\frac{\sigma_0^{VV}}{\sigma_0^{HH}} = A_0+A_1\sin(\phi)+A_2\cos(\phi)+A_3\sin(2\phi)+A_4\cos(2\phi) \tag{6}$$

where ϕ is the angle between wind direction and radar look direction.

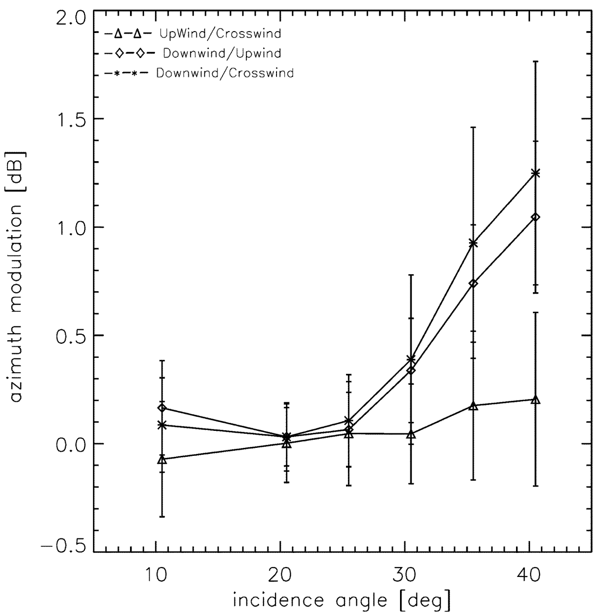

Fig. 8. Modulation depth of the polarization ratio as a function of incidence angle. The modulation depth is calculated between upwind and crosswind directions (solid line with triangles), downwind and upwind directions (solid line with diamonds), and downwind and upwind directions (solid line with stars). Each point corresponds to the mean value calculated over the whole STORM dataset. Vertical bars represent standard deviation with respect to this mean value.

The maximum value of P is observed in the downwind direction, a secondary maximum is found in the upwind direction and minimum values in the two crosswind directions. This is different from the behavior of the NRCS in HH or VV, which is characterized by a maximum in the upwind direction. The same type of modulation of P was already observed at X-band for three cases of observations by Hauser *et al.* [31], and compared to the results of the model of Kudryavtsev *et al.* [11]. It was shown in [11] that the Bragg and two-scale Bragg model were unable to reproduce these modulations. The model proposed in [11], which takes into account wavebreaking was in better agreement with the results of [31]. The same conclusion is found here (not shown).

Fig. 8 illustrates the variation of the azimuth modulation depth of P with incidence angle. It represents the modulation depth of the polarization ratio between upwind and crosswind directions, downwind and upwind directions, and downwind and crosswind directions obtained as a mean value over the whole STORM dataset, and plotted versus incidence angle. We observe that only the downwind/upwind and downwind/crosswind modulations significantly increase with incidence angles for incidences larger than 25°. We also observe that the downwind/crosswind polarization modulation is in average larger than the upwind/crosswind and downwind/upwind modulations. This is due to the larger increase of P with incidence angle in the downwind direction than in the upwind direction. The upwind/crosswind modulation is the smallest in opposite to the well-known modulation of the NRCS in each polarization. This is due to similar values of P in upwind and crosswind directions. These results are in agreement with Unal *et al.* [23] who found similar results at least for the upwind/crosswind ratio at all bands (C-, S-, X-, Ku-band) except L-band, and with measurements at X-band discussed in Hauser *et al.* [33] and Kudryavtsev *et al.* [11].

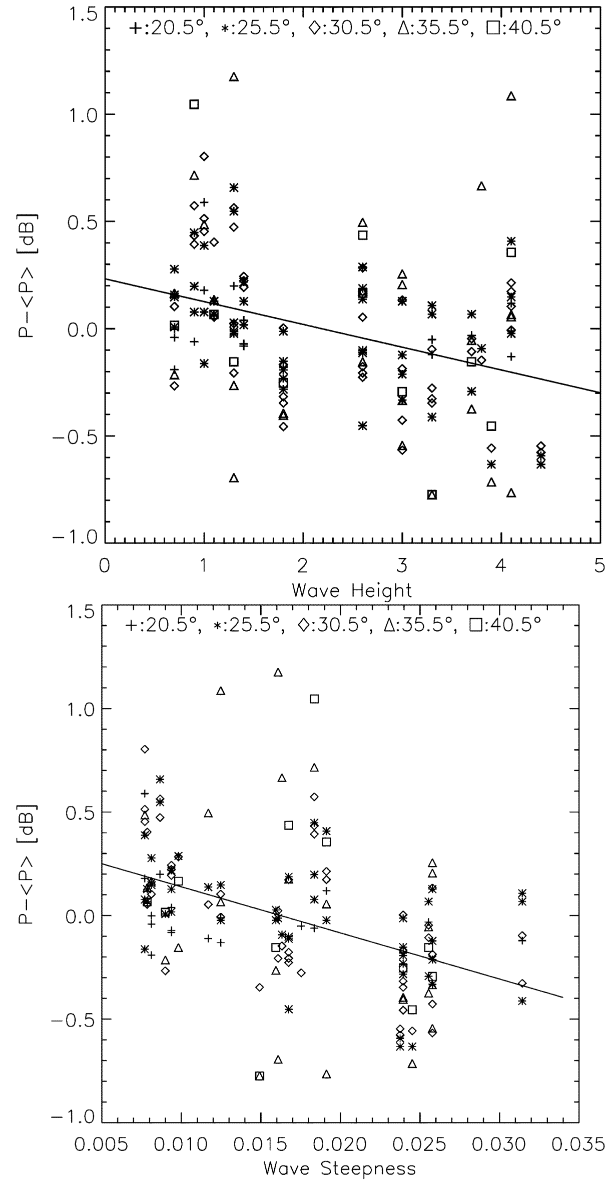

Fig. 9. (a) Deviation of the polarization ratio with respect to its mean value at each incidence angle, as a function of the significant wave height. A different symbol is used for each incidence angle (see on the plot). The linear regression is plotted as the solid line. The correlation coefficient is 0.35 in this case. (b) Same as Fog9a, but as as a function of the significant wave steepness (7). The correlation coefficient is 0.44 in this case.

C. Sea State and Swell Influence

We investigate here below the dependence of the polarization ratio P with sea state conditions. By analyzing the one-dimensional (1-D) spectra of the PHAROS buoy, we found that the sea-state conditions during the VALPARESO campaign were dominated (in more than 70% of the cases) by mixed sea conditions with significant wave heights ranging from 0.7–4.1 m. Hence, we propose to use two parameters to characterize sea state, namely the significant wave height H_s and the significant wave steepness parameter s defined as

$$s = \frac{H_s}{\lambda_p} \tag{7}$$

where λ_p is the peak wavelength estimated from the PHAROS buoy 1-D spectrum, and H_s is the significant wave height calculated over the entire spectrum (swell part and wind sea part).

For the analysis of the correlation with sea-state, we carried out the same analysis as for wind speed, i.e., we estimated the deviation of the polarization ratio with respect to its mean value at each incidence angle. Fig. 9(a) and (b) shows this quantity as a function of wave height and significant wave steepness, respectively. The correlation coefficients are respectively 0.35 and 0.44. A test of null hypothesis based on a random selection of the wave parameters (random procedure repeated 10 000 times) shows that these correlation coefficient values are significative at the 100% confidence level. Hence, it appears that a correlation exists between P-$\langle P\rangle$ and wave parameters and that it is higher than with wind speed (see Section III-B.1). It is also significantly higher for the correlation with significant wave steepness than with significant wave height. The same trend is also observed in the crosswind and downwind directions (not shown here). From these results, we conclude that a dependence of the polarization ratio with wind and wave parameters exist and that the linear correlation is higher with wave steepness than with wave height and wind speed.

Since the significant wave steepness is strongly correlated to the wavebreaking probability (e.g., see [33]), the decrease of the polarization ratio with wave steepness may be explained by an increase of wavebreaking probability with significant wave steepness. As a matter of fact, the model of Kudryavstev *et al.* [11] reproduces, in the case of a pure wind sea, a decrease of the polarization ratio with breaking probability (related in this case to the wind wave spectrum only). This was explained by the contribution of the nonpolarized signal affected by wavebreaking. Here, the results show that the behavior of the polarization ratio is probably more correlated to significant wave steepness than to wind speed. This may also explain the results of Fig. 4, which shows P for two different cases of light wind (4.3 and 4.9 $\mathrm{m\cdot s^{-1}}$), but for which the mean value of P differs by 0.5 to 1.5 dB. In fact, these two cases correspond to similar wind speeds and similar wave height but quite different significant wave steepness (1.6 10^{-2} and 7.7 10^{-3}), due to the presence of short swell in the first case.

D. Polarization Difference

To go further in the analysis of wind and wave influence on the dual-polarized observations, we also examined the behavior of the polarization difference D with wind speed, significant wave height, and significant wave steepness.

If, as proposed for example, by Quilfen *et al.* [34], we express the NRCS as the sum of a polarization-dependent and a scalar term

$$\sigma_0^P = \sigma^{pol} + \sigma^{sc} \tag{8}$$

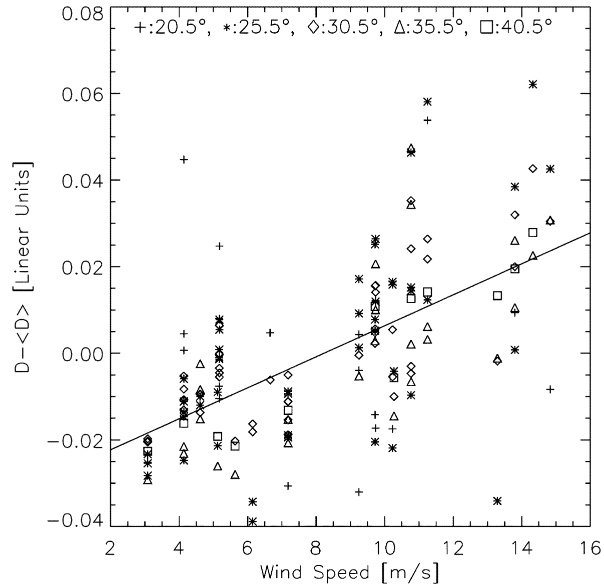

Fig. 10. Deviation from the mean polarization difference (calculated in linear units at each incidence angle) versus wind speed.

then, combining (3) and (8), the polarization difference D becomes

$$D = \sigma_0^{VV} - \sigma_0^{HH} = \sigma^{VV} - \sigma^{HH} \tag{9}$$

where σ^{VV} and σ^{HH} represent the polarized contribution (in VV and HH, respectively) to the radar cross-section.

Thus, the polarization difference D, provides only information on the polarization-dependent terms. For moderate incidence angle (typically 20° to 50°), these polarization-dependent terms are due to Bragg scattering eventually modified by tilt and hydrodynamic effects (e.g., see [11] or [13]).

Fig. 10 shows the deviation of D with respect to its mean value at each considered incidence angle, as a function of wind speed. A clear linear trend is observed. The correlation coefficient is 0.6 in this case, i.e., much larger than that observed for the polarization ratio P [see Fig. 6(b)]. This indicates that the VV-HH difference is related to wind speed. This is expected because of the relation between Bragg backscatter and energy density of short wind waves, in addition to its dependence with incidence angle associated with changes in the Fresnel coefficient (e.g., see [11] or [13]). Tilt and hydrodynamic effects, which are also related to wind intensity and which modify Bragg backscattering, may also influence this polarization difference.

The same analysis carried out for the relation between D and wave parameters indicates that the correlation with these parameters is smaller or even inexistent: correlation coefficient of 0.36 with H_s and 0.02 for wave steepness and the test of null hypothesis on randomized data confirms that there is no correlation with wave steepness. By referring also to the results presented in Section III-B and C, we conclude that the wave steepness s has a very different effect on D and on P: P is correlated with s, but D is not. This means that the wave steepness has a larger influence on the nonpolarized part of the NRCS than on the polarization-dependent terms. Since wave steepness and wavebreaking probability are related [33], this is consistent with recent works [11], [20], which propose to take into account wavebreaking

TABLE IV
COEFFICIENTS OF MODEL 1 [(10) AND (11)]

Coefficient	Fitted values
A_0	0.00650704
B_0	0.128983
C_0	0.992839
$A_{\pi/2}$	0.00782194
$B_{\pi/2}$	0.121405
$C_{\pi/2}$	0.992839
A_π	0.00598416
B_π	0.140952
C_π	0.992885

effects in a non-Bragg additional term, in the modeling of the normalized radar cross-section. Voronovich and Zavarotny [20] also show that their model is consistent with NRCS observations in Ku-band and HH polarization only if a contribution from steep slopes of breakers is accounted for.

To assess these preliminary conclusions about the respective contributions of scalar and polarized terms of the normalized radar cross-section, and about the physical mechanisms which could explain them, we will propose in a future work a joint analysis of our dataset and of different models based on physical backgrounds.

IV. Two New Analytical Models for the Polarization Ratio

As mentioned in the introduction of this paper, SAR images are now commonly used to deduce ocean surface wind fields. For C-band observations in VV (like for ERS and partly ENVISAT), one uses empirical models of CMOD types, which were derived from scatterometer data analysis [1], [2]. For RADARSAT, which is only operating in HH polarization and for the ASAR of ENVISAT, which has a dual-polarization capability, inversion of HH observations to estimate wind speed are still subject to errors due to uncertainty of the empirical models in HH. To progress in the use of C-band HH data, we propose here a simple formulation based on the analysis of our STORM data.

Here below we first propose a model of polarization ratio with two parameters (incidence and azimuth angles). Using such a model requires that the wind direction can be estimated either from the SAR images themselves (following for example the method described in [35] and [36]) or from external data. Then, a simplified model depending only on incidence angle is proposed. The first model is referred to in the following as model 1, the second one as model 2. No attempt has been done to propose a model depending on sea-state, because the dataset that we collected is not sufficient for doing that. Nevertheless as sea state can be estimated from SAR images such a parameterization could be helpful.

Model 1 was built using the following analytical representations. For each incidence angle, the polarization ratio P in linear units is assumed to follow

$$P(\theta, \phi) = C_0(\theta) + C_1(\theta)\cos(\phi) + C_2(\theta)\cos(2\phi). \quad (10)$$

TABLE V
STATISTICAL PARAMETERS FOR THE POLARIZATION MODELS 1 AND 2, WITH RESPECT TO OUR DATASET

		Correlation	Standard deviation	Mean absolute errror
Model 1	All θ	0.99	0.90	0.65
	θ > 30.5°	0.98	1.03	0.77
Model 2	All θ	0.99	0.93	0.67
	θ > 30.5°	0.98	1.08	0.79

In addition, in each azimuth direction, the dependence of P with incidence angle is assumed to follow

$$P_\phi(\theta) = A_\phi \exp(B_\phi\, \theta) + C_\phi. \quad (11)$$

In (10), the C_i coefficients (C_0 to C_2) are related to the polarization ratio P in the three main directions (Upwind $-\phi = 0$ rad, Crosswind $-\phi = \pi/2$ rad, and Downwind $-\phi = \pi$ rad) by

$$C_0(\theta) = \frac{P(\theta,0) + P(\theta,\pi) + 2\,P(\theta,\frac{\pi}{2})}{4} \quad (12a)$$

$$C_1(\theta) = \frac{P(\theta,0) - P(\theta,\pi)}{2} \quad (12b)$$

$$C_2(\theta) = \frac{P(\theta,0) + P(\theta,\pi) - 2\,P(\theta,\frac{\pi}{2})}{4}. \quad (12c)$$

Using the STORM dataset described in Table I, we first calculated from a least square fit, the coefficients $A\phi$, $B\phi$, $C\phi$ in the three main directions (upwind, downwind, crosswind) and then combined the results using (12a)–(12c) to obtain the C_i coefficients of (10). Table IV presents the obtained coefficients. Note that the domain of validity of the resulting analytical model is 10° to 43° for the incidence range (corresponding our range of observations).

The fit of this model is obtained with a correlation coefficient of 0.99, a standard deviation and mean absolute error between data and model of 0.90 and 0.65 dB, respectively (see Table V upper part).

Fig. 11 shows the NRCS in HH as a function of incidence angle, plotted by using model 1 combined with the CMOD2-IFR3 model. Conditions for Fig. 11 are upwind and three different wind speeds (5, 10, 15 $\mathrm{m \cdot s^{-1}}$). The curve for VV polarization according to the CMOD2-IF3 model is also plotted for comparison. The NRCS in HH is smaller than in VV for all incidence angles, and decreases faster than VV-pol with increasing incidence angle. In Fig. 12, HH-pol and VV-pol NRCS are shown versus azimuth angles for a wind speed of 10 $\mathrm{m \cdot s^{-1}}$ and an incidence angle of 40°. Again, the curve for HH is obtained from a combination of our polarization model (model 1) with the CMOD2-IFR3 model, whereas the curve for VV is the CMOD2-IFR3 model. We observe that for all azimuth angles NRCS in HH is smaller than in VV. The upwind-to-crosswind ratio is not very different between HH and VV polarizations (smaller by about 0.5 dB in HH-pol) whereas the upwind-to-downwind is significantly larger in HH as compared to VV, and the downwind-to-crosswind ratio is significantly larger in VV. This is of course consistent with our observations discussed in Section III-B.

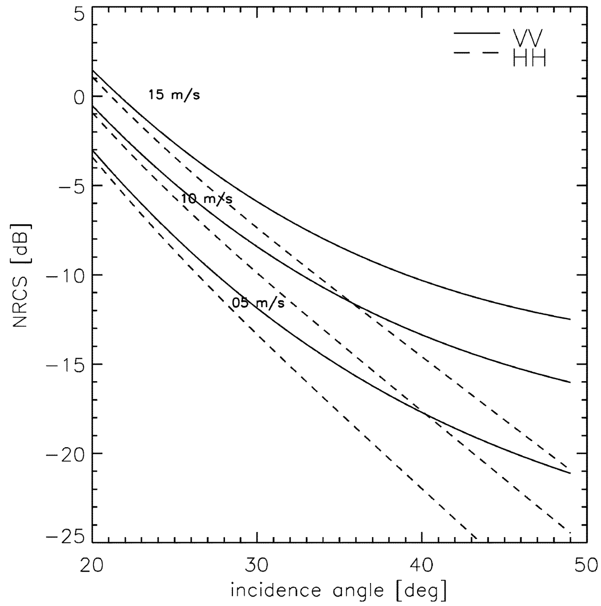

Fig. 11. Normalized radar cross-section versus incidence angle for HH (dotted line) and VV (solid line) and for three wind speeds (5, 10, 15 $\mathrm{m \cdot s^{-1}}$) in the upwind direction. The curve for VV corresponds to the CMOD2-IFR3. The curve for HH is obtained with our hybrid model (CMOD2-IFR3 and model 1 given by (10), (11), and Table IV).

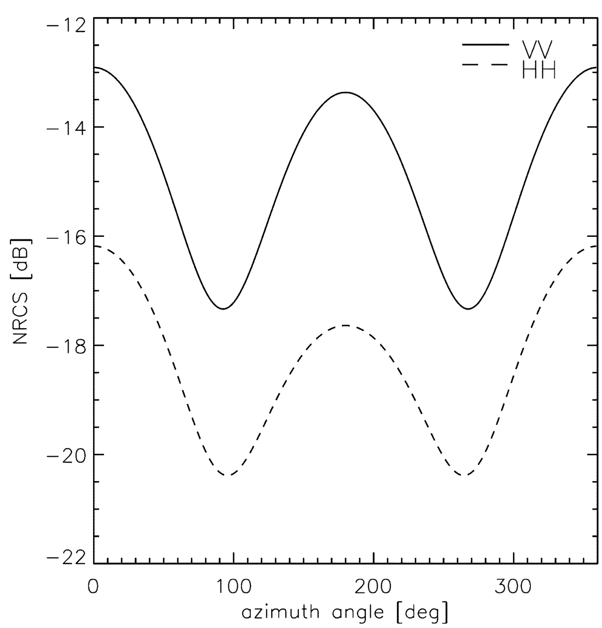

Fig. 12. Normalized radar cross section versus azimuth angle for (dotted line) HH and (solid line) VV polarization. Incidence angle is 40°, wind speed is 10 $\mathrm{m \cdot s^{-1}}$ The curve for VV corresponds to the CMOD2-IFR3. The curve for HH corresponds to our hybrid model (CMOD2-IFR3 and Polarization model 1). On the horizontal axis, 0° represents the upwind direction, and 180° represents the downwind direction.

To our knowledge, all other formulations proposed in the literature to model the polarization ratio do not use the azimuth angle as a variable (e.g., [6]–[8]). Here, model 1 is the first one proposed, which accounts for the azimuth variation of the polarization ratio. To compare with the other formulations in the literature and also because it is not always possible to know the wind direction associated to SAR observations, we also built a second model, hereafter referred to as model 2, without considering azimuth angles dependencies. In this case, we express the polarization ratio as

$$P(\theta) = A\exp(B\theta) + C, \qquad \text{[linear units]} \qquad (13)$$

with A, B, and C constant coefficients.

As for model 1, coefficients A, B, C have been estimated from a fit of (13) on the observed values of P in the directions upwind, downwind, and crosswind. Table VI gives the corresponding coefficient, and Table V (bottom part) gives the correlation coefficient, standard deviation, and mean absolute error between this model and the observations. Compared to model 1, model 2 has a slightly weaker performance in terms of standard deviation and mean absolute error. These larger uncertainties are more pronounced on the statistical parameters calculated for incidence angles larger than 30.5° (see Table V). Therefore, we may conclude that model 1 provides a better representation of our dataset than model 2.

TABLE VI
COEFFICIENTS OF MODEL 2 (13)

Coefficient	Fitted values
A	0.00799793
B	0.125465
C	0.997379

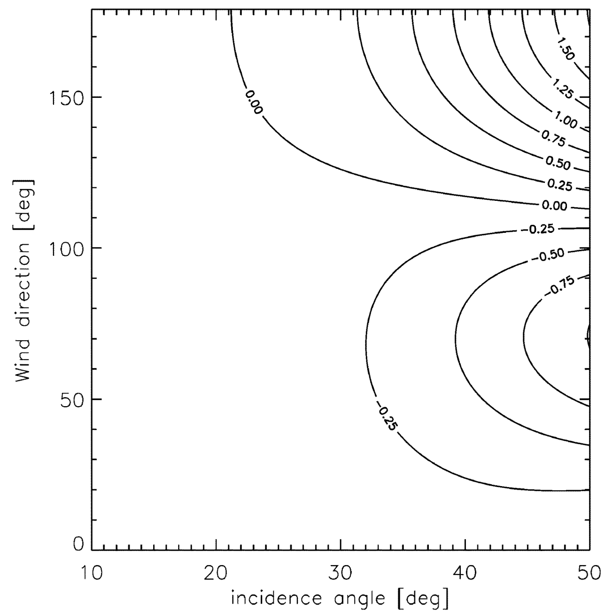

Fig. 13. Difference between model 1 and model 2 for the polarization ratio (in decibels). The difference is plotted as a function of incidence angle and wind direction (from 0° to 180° only because of the symmetry from 180° to 360°) as contour every 0.25 dB (first contour at 0 dB).

V. DISCUSSION

To characterize the difference in the proposed models (1 and 2), we calculated and plotted (Fig. 13) the difference of the polarization ratio (in decibels) as a function of incidence angle and azimuth angle (angle between wind direction and radar look direction). Due to symmetry in the [0° to 360°] range of azimuth angles, Fig. 13 shows results in the [0° to 180°] range only.

The difference between model 1 and model 2 increases with incidence angle and becomes significant (> 0.2 dB in absolute values), for incidence angles larger than 30°. Positive differences are found for azimuth angles in the range [110° to 180°] (and [180° to 290°] for the symmetric part). The maximum positive difference (model 1 minus model 2) is 1.75 dB and is observed in the downwind direction for the largest incidence angles (50°). This is due to the azimuth modulation of model 1, which is maximum in the downwind direction and increases with incidence angle. Negative differences are found between 0° and 110° (and between 290° and 360° for the symmetric part). The maximum negative difference is -1 dB and is reached for an azimuth direction of 70° $(\pm 180^\circ)$ and the largest incidence angle (50°). The smallest difference between models 1 and 2 is obtained near the crosswind direction (100°).

From this analysis we conclude that up to an incidence angle of 30°, model 2 is probably accurate enough (error less than ±0.2 dB). In opposite, we recommend that at large incidence angles (larger than 30°), model 1 be used for the polarization ratio, because model 2 could induce a significant error at large incidence (up to 1.5 dB for 45°). For a 10-ms^{-1} wind speed, such an error can lead to a 2-m·s^{-1} error on wind speed retrieval.

We now consider the hybrid model composed of the polarization ratio Model 1 combined with the CMOD2-IF3 model. This hybrid model can be applied on observed HH-polarized NRCS

$$\sigma_{VVEqu} = P(\theta, \phi)\sigma_{HHobs}. \tag{14}$$

This hybrid model is used below to estimate the impact of wind direction error on wind speed retrieved through (14) combined with CMOD2-IFR3, and assuming σ_{HHobs} values are free of error. The method is similar to the one proposed and used in [7], [35], and [36]. The results at small incidence angle (23°) indicate that the relative error on the retrieved wind speed due to an error on wind direction does not depend on the choice of the polarization model. Indeed same kind of errors are found when model 1 or when model 2 or model of [6] are used for P (not shown). A different conclusion is reached when examining the results at larger incidence (43°). In this case [Fig. 14(a) and (b)], the errors on wind speed are significantly different when calculated with our hybrid model [Fig. 14(a)] or when calculated with a hybrid model without azimuth dependency [Fig. 14(b)]. They are smaller in the former case, especially in the two directions of the maximum of error $(65^\circ \pm 180^\circ)$, and 125° $(\pm 180^\circ)$, and there is a significant asymmetry between these two directions in terms of error (maximum values of 14% at 125° ± 180°, and 20% at 65° ± 180°). This asymmetry comes from a compensating effect of inversed sensitivity of the CMOD2-IFR3 model and of the polarization model with azimuth angle.

In summary, our hybrid model compared to classical ones, which do not take into account variation with azimuth of the polarization ratio, leads to smaller errors on wind speed for an expected error on wind direction. But this difference is only significant for incidence angles larger than 30°.

VI. Validation of the Proposed Models With Envisat Asar Observations

In the following, we consider the ENVISAT dataset of Table III acquired in the alternating polarization mode (HH and VV) to assess our formulation. Data were provided by ESA as single-look complex products (APS). They correspond to 23 images (of about 100 km dimension along-track), corresponding to nine different days and areas. The incidence range covered by these images is 18° to 45°. Note that, an absolute calibration factor is not needed when using these data to calculate the polarization ratio. According to the surface fields provided by the ECMWF meteorological analysis, the corresponding wind speed ranges from 1–16 m · s^{-1}.

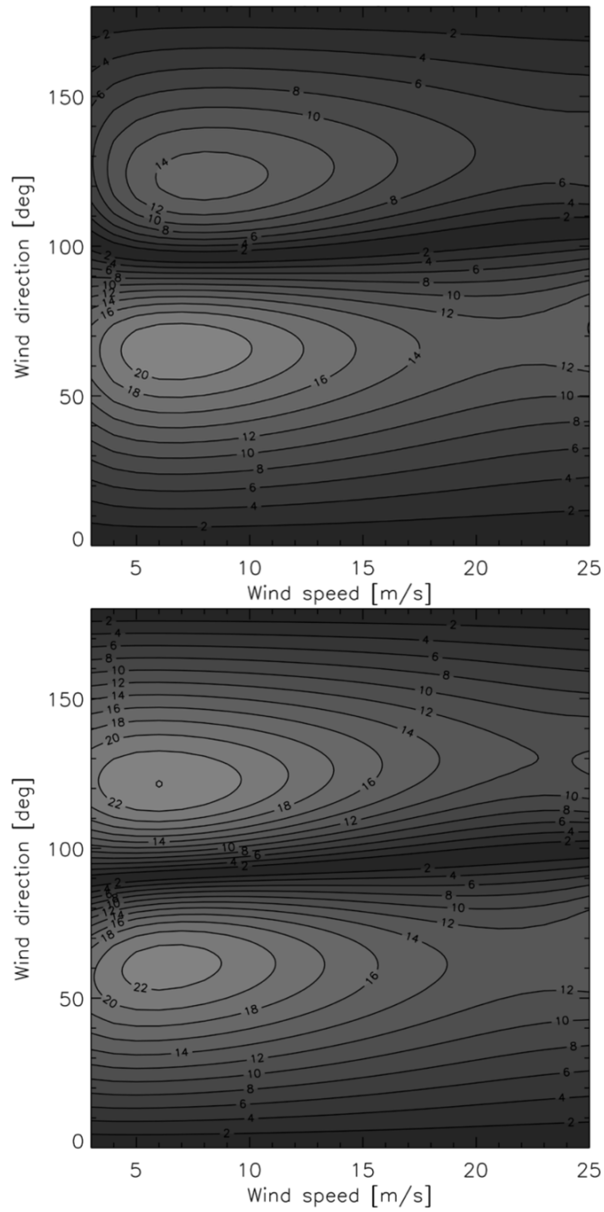

Fig. 14. (a) Relative error with our hybrid model 1, in percentage of wind speed, due to an error of $\pm 10^\circ$ on the wind direction and for the incidence angle of 43°, 0° and 180° on the vertical axis correspond respectively to the upwind and downwind directions. (b) Same as (a), but for the CMOD2-IFR3 model or hybrid model which does not take into account the azimuth dependence.

Fig. 15 shows the polarization ratio from the ASAR versus incidence angle compared to 4 models: the formulations from Thompson *et al.* [6] [(4)] with $\alpha = 0.6$, from Vachon and Dobson [8] with $\alpha = 1$, from Elfouhaily [24], and model 1 of this study. In this latter case curves for crosswind and downwind

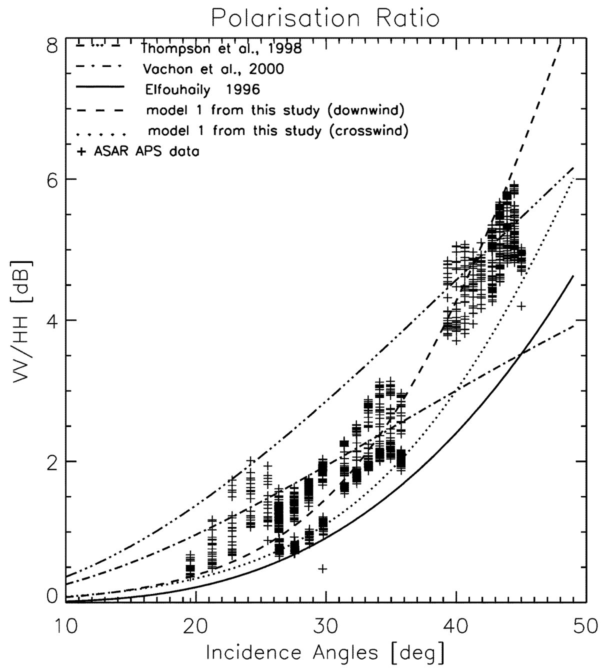

Fig. 15. Polarization ratio as a function of incidence angle, from the ASAR dataset of Table IV (crosses), and from various formulations, as indicated in the figure.

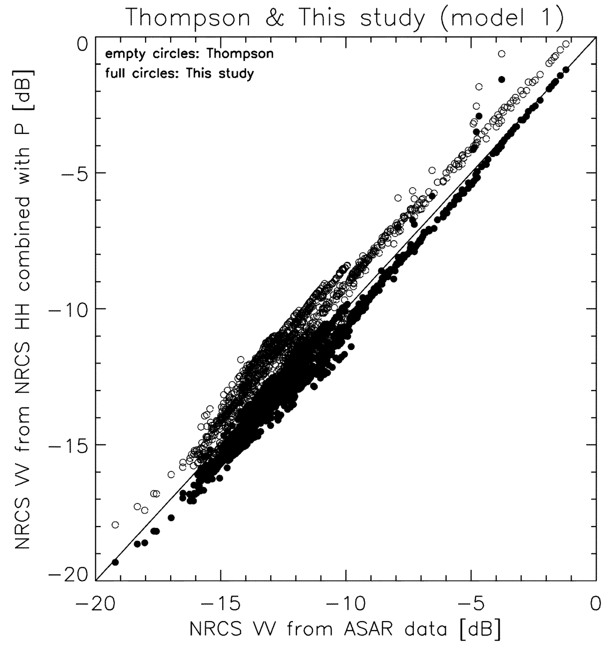

Fig. 16. Observed normalized radar cross section in VV polarization from ASAR measurements versus equivalent values calculated from observed HH-polarized data of the same scene combined with our polarization model 1 (black circles), and with the model of [6] (open circles).

are plotted, corresponding respectively to the minimum and maximum values of the model. Formulation [6] is in agreement with ASAR data only for the largest incidence angles whereas it overestimates the polarization ratio for incidence angles smaller than 40°. In opposite, the formulation from Vachon and Dobson [8] is in rather good agreement for incidence angles smaller than 40° but underestimates the polarization ratio for larger incidence angles. Elfouhaily's expression has a correct trend with incidence angle but underestimates the polarization ratio over the whole range of incidence. Finally, our model 1 is close to the data for the whole range of incidence angles. Furthermore, it allows a variation with azimuth angle for a given incidence angle, in consistency with the observations.

Pixel by pixel comparisons were also performed between the VV-NRCS measured by ASAR against its equivalent counterpart using (14) and five different polarization models ([6], [8], [24], and our models 1 and 2). For the comparisons with model 1, the azimuth direction was fixed from the wind surface fields of the ECMWF analysis. The results are summarized in Table VII, and illustrated in Fig. 16 for two models (model 1 of this study, and model [6]). For all models, the correlation coefficient is quite high (larger than 0.9) but it is the highest with our models 1 and 2. The rms difference between models and observation is the smallest for our models (1 and 2). The smallest bias (mean error between model and observations) is obtained with our model 1 and model [8]. However, the scatter plot for model [8] (not shown) indicates that this small bias is in fact due to a compensating effects of a positive and negative bias for NRCS respectively above and below −9 dB. This is confirmed by the mean absolute error, which is the smallest for model 1. Model [6] shows the largest bias with respect to the data (mean error 0.85 dB). In summary, the polarization ratio from the ASAR APS data is in better agreement with our formulations and especially with our model 1 (which takes into account azimuth direction) compared to the other proposed models. Contradiction of this conclusion with some previous works may appear, but it may be due to the fact that our approach is independent of an absolute calibration error of radar cross-sections, whereas previous work based on the analysis of HH-polarized RADARSAT data may be affected by a calibration uncertainty.

VII. Conclusion

In this paper, we analyzed the polarization ratio (ratio of the normalized radar cross-sections in VV and HH polarizations) from airborne measurements performed with the STORM radar during the VALPARESO experiment. Coincident ASAR images of the ENVISAT satellite were also used to assess our results. The results confirm that the polarization ratio is dependent on the incidence angle but show that the existing formulations [6]–[9] are not consistent with our dataset. Theoretical models [11], [24] are in reasonably good agreement with our observations, whereas a two-scale Bragg model cannot reproduce these observations. The optical approximation is valid only up to incidence angles of about 20°. We have also shown that the polarization ratio is a function of the azimuth angle between wind direction and radar direction. Modulations of the polarization ratio with azimuth can be represented by a second-order Fourier series, with first maximum corresponding to downwind direction, the second to upwind direction whereas the two minima correspond to crosswind directions. This azimuth modulation of the polarization ratio increases with incidence angles but is negligible for incidence angles less than 30°.

The data revealed also that the polarization ratio P is dependent on surface conditions, but much more on wave steepness

TABLE VII
MEAN ERROR AND RMS (CALCULATED IN DECIBELS) BETWEEN VV-POL NRCS PREDICTED FROM ASAR HH-NRCS MEASUREMENTS WITH FIVE DIFFERENT POLARIZATION MODELS, AND VV-POL NRCS MEASURED BY ASAR

	Correlation	Rms (dB)	Mean error (dB)	Mean absolute error (dB)
Model 1 (this study)	0.99	0.41	-0.39	0.47
Model 2 (this study)	0.98	0.47	-0.52	0.57
Thompson *et al.,*1998 [6] : α=0.6	0.97	0.63	0.85	0.92
Vachon and Dobson [8]: α=1.0	0.94	0.99	-0.32	0.78
Elfouhaily, 1996 [24]	0.97	0.78	-1.01	1.06

than on wave height and wind speed. A preliminary interpretation of these results combined with those obtained on the polarization difference D, leads us to conclude that wave steepness is a key parameter for the scalar part of the backscattering mechanism. Since wave steepness and wavebreaking statistics are likely related, this observation confirms theories developed by Voronovich and Zavarotny [20] or Kudryavtsev *et al.* [11] which provide results consistent with observations only when wavebreaking is taken into account. Furthermore, observations of polarization ratio and/or difference could be used in the future to estimate some wave steepness and/or wavebreaking parameter.

From the dataset, we built two simple analytical models of the polarization ratio. The first one (model 1) depends on azimuth and incidence angles whereas the second one (model 2) depends on incidence only. Both reproduce the trend of the data with incidence angles, in opposite to other models available in literature. Comparisons between both models show that up to 30° incidence angle, model 2 could be used because of the weak azimuth angle dependence at small to moderate incidences. But for large incidences ($> 30^\circ$) the azimuth dependence (i.e., model 1) should be considered to avoid significant errors on VV-pol NRCS prediction and then on wind speed (up to 2 $\mathrm{m \cdot s^{-1}}$ at large incidence angles and for a 10-$\mathrm{m \cdot s^{-1}}$ wind speed).

This polarization ratio model, combined with the CMOD2-IFR3 available for VV polarizations observations forms a new hybrid model, which can be used to invert HH-pol in terms of wind speed. Comparisons with others hybrid models which do not take into account the azimuth variation of the polarization ratio, show that our model is less sensitive to wind direction uncertainties.

Finally, comparisons with APS ASAR data showed that our azimuth-dependent polarization ratio formulation give the best results to predict VV-pol NRCS data from HH-pol NRCS data.

For all these reasons, we recommend here to use our formulation (model 1) of the polarization ratio.

Future work will be devoted to propose a physical interpretation of the present results by combining them to models based on physical backgrounds such as those proposed in [11], [20], and [37].

ACKNOWLEDGMENT

The authors would like to thank all the technical staff who participated in the VALPARESO campaign, and in particular the aircraft team from Météo-France, and the technical staff of CETP in charge of the radar instrument and processing (T. Podvin, L. Chardenal, F. Boutet). The data from PHAROS buoy have been provided by Météo-France (J-P Jullien, P. Blouch). The ECMWF wind fields used to estimate wind direction in one of the ASAR dataset, was provided by IPSL (S. Cloché). The authors thank their colleagues A. Protat and G. de Coëtlogon for helpful comments for the revision of the manuscript.

REFERENCES

[1] A. Stoffelen and D. Anderson, "Scatterometer data interpretation: Estimation and validation of the transfer function CMOD4," *J. Geophys. Res.*, vol. 102, pp. 5767–5780, 1997.
[2] A. Bentamy, P. Queffeulou, Y. Quilfen, and K. Katsaros, "Ocean surface wind fields estimated from satellite active and passive microwave instruments," *IEEE Trans. Geosci. Remote Sens.*, vol. 37, no. 5, pp. 2469–2486, Sep. 1999.
[3] F. J. Wentz, S. Peteherich, and L. A. Thomas, "A model function for ocean radar cross-section at 14.6 GHz," *J. Geophys. Res.*, vol. 89, pp. 3689–3704, 1984.
[4] F. J. Wentz and D. K. Smith, "A model function for the ocean-normalized radar cross section at 14 GHz derived from NSCAT observations," *J. Geophys. Res.*, vol. 104, pp. 11 499–11 514, 1999.
[5] R. K. Raney, A. P. Luscombe, E. J. Langham, and S. S. Ahmed, "RADARSAT," *Proc. IEEE*, vol. 79, no. 6, pp. 839–849, Jun. 1991.
[6] D. R. Thompson, T. M. Elfouhaily, and B. Chapron, "Polarization ratio for microwave backscattering from the ocean surface at low to moderate incidence angles," in *Proc. IGARSS*, Seattle, WA, 1998.
[7] J. Horstmann, W. Koch, S. Lehner, and R. Tonboe, "Wind retrieval over the ocean using synthetic aperture radar with C-band HH polarization," *IEEE Trans. Geosci. Remote Sens.*, vol. 38, no. 5, pp. 2122–2131, Sep. 2000.
[8] P. W. Vachon and F. W. Dobson, "Wind retrieval from RADARSAT SAR images selection of a suitable C-band HH polarization wind retrieval model," *Can. J. Remote Sens.*, vol. 26, no. 4, pp. 306–313, 2000.
[9] F. M. Monaldo, D. R. Thompson, R. C. Beal, W. G. Pichel, and P. Clemento-Colon, "Comparison of SAR-Derived wind speed with model predictions and ocean buoy measurements," *IEEE Trans. Geosci. Remote Sens.*, vol. 39, no. 12, pp. 2587–2600, Dec. 2001.
[10] C. C. Wackerman and P. Clemente-Colon, "A two scale model to predict C-band VV and HH normalized radar cross section values over the ocean," *Can. J. Remote Sens.*, vol. 28, no. 3, pp. 367–384, 2002.
[11] V. Kudryavtsev, D. Hauser, G. Caudal, and B. Chapron, "A semi-empirical model of the normalized radar cross section of the sea surface, 1.Background model," *J. Geophys. Res.*, vol. 108, 2003.
[12] W. J. Plant, "Microwave sea return at moderate to high incidence angles," *Waves Random Media*, vol. 9, pp. 339–354, 2003.
[13] ——, "A two scale model of short wind-generated waves and scatterometry," *J. Geophys. Res.*, vol. 91, pp. 10,735–10 749, 1986.
[14] M. A. Donelan and W. J. Pierson, "Radar scattering and equilibrium ranges in wind-generated waves," *J. Geophys. Res.*, vol. 92, pp. 4971–5029, 1987.
[15] R. Romeiser, A. Schmidt, and W. Alpers, "A three-scale composite surface model for the ocean wave-radar modulation transfer function," *J. Geophys. Res.*, vol. 99, pp. 9785–9801, 1994.
[16] R. Romeiser and W. Alpers, "An improved composite surface model for the radar backscattering cross section of the ocean surface: Model response to surface roughness variations and the radar imagery of underwater bottom topography," *J. Geophys. Res.*, vol. 99, pp. 9785–9801, 1997.
[17] P. A. E. M. Jannsen, H. Wallbrink, C. J. Calkoen, D. Van Halsema, W. A. Oost, and P. Snoeij, "VIERS-1 scatterometer model," *J. Geophys. Res.*, vol. 103, pp. 7807–7831, 1998.

[18] G. R. Valenzuala, "Theories for the interactions of electromagnetic and oceanic water—A review," in *Bound. Layer Meteorol.*, 1978, vol. 13, pp. 177–187.

[19] W. J. Plant, "Bragg scattering of electromagnetic waves from air/sea interface," in *Surfaces, Wave, Fluxes and Remote Sensing*, G. L. Gernaert and W. J. Plant, Eds. Dordrecht, The Netherlands: Kluwer, 1990, vol. 2, pp. 41–108.

[20] A. G. Voronovich and V. U. Zavorotny, "Theoretical model for scattering of radar signals in K_u- and C-bands from a rough sea surface with breaking waves," *Waves Random Media*, vol. 11, pp. 247–269, 2001.

[21] W. J. Plant, W. C. Keller, V. Hesany, T. Hara, E. Bock, and M. Donelan, "Bound waves and Bragg scattering in a wind-wave tank," *J. Geophys. Res.*, vol. 104 , no. C2, pp. 3243–3263, 1999.

[22] W. J. Plant, "Microwave sea return at moderate to high incidence angles," *Waves Random Media*, vol. 13, pp. 339–354, 2003.

[23] C. M. H. Unal, P. Snoeij, and P. J. F. Swart, "The polarization-dependent relation between radar backscatter from the ocean surface and surface wind vector at frequencies between 1 and 18 GHz," *IEEE Trans. Geosci. Remote Sens.*, vol. 29, no. 4, pp. 621–627, Jul. 1991.

[24] T. M. Elfouhaily, "Modèle couple vent/vagues et son application à la télédétection par micro-onde de la surface de la mer," Ph.D. thesis (in English), Univ. Paris VII, Paris, France, 1996.

[25] D. Hauser, T. Podvin, M. Dechambre, R. Valentin, G. Caudal, and J.-F. Daloze, "STORM: A new polarimetric real aperture radar for earth observations," presented at the *ESA Int. POLinSAR Workshop on Applications of SAR Polarimetry and Polarimetric Interferometry*, http://earth.esa.int/polinsar/participants/hauser4/POLINSAR-STORM.pdf.

[26] J.-P. Chalon, M. André, J.-L. Brenguier, A. Druilhet, J.-F. Gayet, P. Flamant, B. Guillemet, D. Hauser, Y. Kerr, J. Pelon, M. Ravaut, and D. Tanré, "Les avions français de recherche atmosphérique et de télédétection: Bilan et perspectives," *La Météorol.*, vol. 8, no. 22, pp. 14–44.

[27] D. Hauser, G. Caudal, G.-J. Rijckenberg, D. Vidal-Madjar, G. Laurent, and P. Lancelin, "RESSAC: A new airborne FM/CW radar ocean wave spectrometer," *IEEE Trans. Geosci. Remote Sens.*, vol. 30, no. 5, pp. 981–995, Sep. 1992.

[28] F. T. Ulaby, R. K. Moore, and A. K. Fung, *Microwave Remote Sensing and Surface Scattering and Emission Theory*. Reading, MA: Addison-Wesley, 1982.

[29] O. M. Phillips, "Spectral and statistical properties of the equilibrium range in the wind-generated gravity waves," *J. Fluid Mech.*, vol. 156, pp. 505–531, 1985.

[30] F. J. Wentz and D. K. Smith, "A model function for the ocean-normalized radar cross-section at 14 GHz derived from NSCAT observations," *J. Geophys. Res.*, vol. 104-C5, pp. 11 499–11 514, 1999.

[31] D. Hauser, P. Dubois, and G. Caudal, "Polarimetric wind-scatterometer measurements during the Polrad'96 Experiment," ESA, Noordwijk, The Netherlands, Final Report of ESA Contract No. OP/WK/336073, 1997.

[32] C. W. Fairall, E. F. Bradley, D. P. Rogers, J. B. Edson, and G. S. Young, "Bulk parameterization of air-sea fluxes for TOGA COARE," *J. Geophys. Res.*, vol. 101, pp. 3747–3767, 1996.

[33] J. H. G. M. Alves and M. L. Banner, "Performance of a saturation-based dissipation-rate source term in modeling the fetch-limited evolution of wind waves," *J. Phys. Oceanography*, vol. 33, pp. 1274–1298, Jun. 2003.

[34] Y. Quilfen, B. Chapron, A. Bentamy, J. Gourrion, T. M. Elfouhaily, and D. Vandermark, "Global ERS 1 and 2 NSCAT observations: Upwind/crosswind and upwind/downwind measurements," *J. Geophys. Res.*, vol. 104, pp. 11 459–11 469, 1999.

[35] J. Hortsmann, S. Lehner, W. Koch, and R. Tonboe, "Computation of wind vectors over the ocean using spaceborne synthetic aperture radar," in *John Hopkins Tech. Dig.*, vol. 21, 2000.

[36] S. Lehner, J. Horstmann, W. Koch, and W. Rosenthal, "Mesoscale wind measurements using recalibrated ERS SAR images," *J. Geophys. Res.*, vol. 103, pp. 7847–7856, 1998.

[37] T. Elfouhaily, S. Guignard, R. Awadallah, and D. R. Thompson, "Local and non local curvature approximation: A new asymptotic theory for wave scattering," *Waves Random Media*, vol. 13, pp. 321–337, 2003.

Alexis A. Mouche received the D.E.A. degree (Master degree) in the physics for remote sensing from the University of Paris, Paris, France, in 2002.

He joined the Centre d'Étude des Environnements Terrestres et Planétaires (CETP), Velizy, France, in 2002 as a Ph.D. student in the remote sensing team. His current research field is in the study of the ocean surface by active microwave sensors.

Danièle Hauser was born in Grenoble, France, in 1955. She received the Ph.D. Degree in physics (speciality meteorology) in 1980 and a Thèse d'Etat in 1989 on cloud physics from the University of Paris VII, Paris, France.

She became a Researcher of the French National Centre for Research (CNRS) in 1982, working at that time on cloud physics from Doppler radar measurements at CRPE (former name of CETP). Since 1989, her research work deals with remote sensing of the ocean surface and air–sea interactions and is carried out at the Centre d'Etude des Environnements Terrestres et Planétaires (CETP), a joint laboratory of CNRS and the University of Versailles-Saint-Quentin-en-Yvelines. She became a Senior Researcher (Directeur de Recherches) of CNRS in 1995. She has been the Leading Scientist of several experimental projects (airborne radar RESSAC, STORM) or field experiments (FETCH, VALPARESO) and has participated in several other international projects (SWADE, SEMAPHORE, ERS validation, etc.). She is author or coauthor of about 40 papers in journals and of about 50 proceedings of international conferences.

Jean-François Daloze received the Master degree in geophysics from the University of Strasbourg, Strasbourg, France, in 2002.

He has been working at the Centre d'Etude des Environnements Terrestres et Planétaires, Velizy, France, from 2002 to 2004 on the STORM radar data postprocessing

Christine Guréin received the Ph.D. degree in geophysics from the University of Paris VI, Paris, France, in 1970.

She is currently a Research Engineer with the Centre d'Etude des Environnements Terrestres et Planétaires, Velizy, France, working on software developments for earth observations studies.